SPE-183298-MS

Positive Displacement Motor Modeling: Skyrocketing the Way We Design, Select, and Operate Mud Motors

Samba BA, Maxim Pushkarev, Anton Kolyshkin, Lijun Song, and Ling Ling Yin, Schlumberger

Copyright 2016, Society of Petroleum Engineers

This paper was prepared for presentation at the Abu Dhabi International Petroleum Exhibition & Conference held in Abu Dhabi, UAE, 7-10 November 2016.

This paper was selected for presentation by an SPE program committee following review of information contained in an abstract submitted by the author(s). Contents of the paper have not been reviewed by the Society of Petroleum Engineers and are subject to correction by the author(s). The material does not necessarily reflect any position of the Society of Petroleum Engineers, its officers, or members. Electronic reproduction, distribution, or storage of any part of this paper without the written consent of the Society of Petroleum Engineers is prohibited. Permission to reproduce in print is restricted to an abstract of not more than 300 words; illustrations may not be copied. The abstract must contain conspicuous acknowledgment of SPE copyright.

Abstract

We present in this paper a comprehensive and universal tool/model for the mud motor power section. The model includes performance, fatigue, and hysteresis heating simulation capability. It can be used for improved and optimized power section design, motor selection prior to jobs, drilling parameters optimization, failures analysis, and training. Model predictions are compared with real field cases with good accuracy.

There are many challenges to build a proper model of the power section: a geometry that involves complex kinematics with progressive cavities moving in a spiral motion, unusual contact mechanism with high deformation from the elastomer, the elastomer itself being a highly nonlinear material that experiences hysteresis heating, the fluid aspect with complex 3D path, the interaction between the fluid and the elastomer, the sliding and rotating operating modes, and the load fluctuation in typical downhole instable conditions. To build an adequate model we have developed a set of modules with a unique apparatus helping to make cross-interacting links between them.

The present simulation capability allows us to predict the performance and the fatigue life of the power sections with good precision. We have already run many different power section simulations under different conditions showing good correlation with field data. We provide here direct field operation applications with comparative results between some field failures and model predictions. In addition, we expose how combining accurate profile measurements of the rotor and the stator with the modeling capability can prevent failures due to wrong interference fit or incompatibility between rotors and stators. Besides that, a comparative study with different elastomers in the same power section is also considered. We show also how we can use the model for well planning by selecting the right motor for the right application. Moreover, during the well execution, by combining its prediction and the monitoring system to derive optimized drilling parameters for performance and reliability, one can achieve higher shoe-to- shoe rate of penetration (ROP).

Introduction

Progressive cavity pumps (PCP) and positive displacement motors (PDM) are used worldwide in drilling vertical and directional wells for oil and gas exploration, appraisal, and production. It is believed that

over 60% of all directional drilling (DD) runs are performed with PDMs. A few unique features in PDM design make them a very popular product. First, the universality of mud motors allows drilling with them independently even for complex well trajectories or they can be easily combined with the most advanced rotary steerable system (RSS) to enhance drilling performance. Second, the power density delivered by the PDM tool remains unbeatable compared with alternative technologies such as turbines, downhole electrical motors, etc. Third, the cost of PDM tool manufacturing is significantly less than that of an RSS, and its maintenance procedure is simpler than for an RSS.

Power section assemblies are the most critical part of the mud motors (Tiraspolsky 1985). Although the first concept of the PCP/PDM mechanism was suggested many decades ago (Moineau 1931), demands are still high for motors with improved performance and durability. Despite the seemingly simplicity of power section design, incredibly complex multiple physics processes are occurring while the power section works. A solid and comprehensive methodology/tool is required to design power sections and use them optimally downhole.

A power section consists of a rotor and stator pair, which converts the hydraulic energy of pressurized fluid into mechanical energy on a rotating shaft. It is typically categorized by its size, number of lobes, and number of stages. When fluid moves through the rotor and the stator, pressure differences between the enclosed cavities cause the rotor to rotate inside the stator. Ideally, the cavities are sealed from each other; however, when the pressure is high enough to break the sealing between the moving cavities, part of the fluid starts to slip through cavity boundaries. A relatively small amount of slippage can be beneficial because it reduces friction and wear by lubricating and cooling the rotor and the stator, whereas a large amount of slippage reduces the effective volumetric efficiency and increases erosive wear if the pressure between adjacent cavities is too high and can even lead to motor stalling.

In addition, it is fair to say that the reduced power section efficiency and the elastomer erosion are not the only issues that become severe with high differential pressure. The repeated elastomer deformation is responsible for fatigue crack growth and hysteresis heating, which might ultimately lead to the most common motor failure—elastomer chunking.

In this paper, a new modeling methodology to simulate mud motor power generation, fatigue life, and hysteresis heating is exposed. It uses a combination of both modeling and testing.

After a quick literature review, we will expose the full methodology by highlighting the different parts that composed it, and then we will talk about the results and the application of the methodology. In particular, we will show how one can use this capability to design better power sections, select the right power sections for the right application, and operate them optimally for enhanced performance and reliability.

Literature Review

To understand existing tool performance and risk of failures, a large collection of field runs is often required. Yanez et al. (2013) gave an overview of using good data sets to understand power section failures. Laboratory testing has been used frequently to validate a design concept (Olivet et al. 2002; Mirza 2007; Dunn and Prakash 2014). Gamboa et al. (2003) employed analytical correlations to relate the leakage flow to geometrical parameters such as the interference between the rotor and the stator as well as fluid viscosities. Delpassand (1999) used a finite element analysis (FEA) approach to evaluate the hysteresis heat buildup for failure analysis in a stator elastomer. Three-dimensional computational fluid dynamics (CFD) have been employed on motors with single-lobe geometries (Paladino et al. 2008; Andrade et al. 2011; Berton et al. 2011; de Azevedo et al. 2016). In similar geometry setups, the method of finite element modeling can be combined with fluid solid interactions to compute the torque and volumetric efficiency (Lima et al. 2013; Chen et al. 2014). In the above simulations, a continuous gap between the stator and rotor must be maintained to form a continuous non-interruptive fluid domain. Although theoretical correlations with simplified assumptions and computations with relatively simple geometries have been proved useful to understand the PDM motor behavior, more detailed analyses are required in complex situations, including

high-lobe-number geometries in which the rotor and the stator may also have full or partial contacts. The deformed geometries may significantly affect the flow with localized change in gap and contact (no gap) between the rotor and the stator. Truly, what is really needed is a fluid structure interaction (FSI) model, which would apply the deformed geometry to the fluid domain and vice-versa.

The kinematics of the power section is complex and comprises eccentric motion of the rotor inside the stator with the shape of the movement describing a combination of hypocycloids and epicycloids. In 2006, a working group of 16 mathematicians from Denmark Technical University (DTU) took on a task for describing mathematically the power section profiles and the motions involved (Aage et al. 2006). Their work is tremendous, and they were able to derive closed form equations for some of the designed profiles of rotors and corresponding stators. However, they did not make any effort on the kinetics aspects and the calculation of the forces or mechanical properties of the different designs considered.

A team led by D.F. Baldenko conducted another great academic study of mud motors. It was published in Russia in 2005 as a two-volume engineering book (Baldenko et al. 2005). It tackles many theoretical aspects related to the profiling, the kinematics, and the optimization of both PDM and PCP mechanisms. An English adaptation of this work was done by Robello et al. (2015). Both publications are comprehensive and very useful from a theoretical point of view. However, the authors did not consider some aspects related to the FEA/CFD/FSI modeling.

The performance of any PCP/PDM mechanism depends very much on the leakage between the stator and the rotor. A certain number of works deal with this subject; see articles by Noble and Dunn (2011), Andrade et al. (2010), Bratu (2005), and Ramasamy and Samad (2011), for example. However, the information in these investigations is mainly related to the specificity of PCPs. Stator/rotor interactions in PDM power sections are slightly more complex and often require additional efforts; usually, the number of lobes is much higher in PDMs compared to PCPs and often in PDMs, there are extra fluctuations in loading mechanisms.

In summary, all known publications related to the mud motor modeling are to some degrees partial, usually dealing with only one aspect of the motor physics (hysteresis, flow leakage, rotor kinematics, etc.) and often using a simplified one-lobe configuration. So far, we could not find a comprehensive, fully scalable model taking into account many physical factors at the same time. In fact, there is a high demand for a model that can predict mud motor behavior in terms of performance and reliability at the same time.

The purpose of the current work is to develop such model with its related testing methodology. The pursued model must take into account operating parameters, real rotor/stator geometry, material properties, thermal effects, and chemical and physical interaction with mud. As output, the model must predict accurately motor performance (power curves) and reliability (fatigue life, hysteresis heating). The entire methodology combining both testing and modeling is described herein.

Modeling Methodology

As mentioned before, the complexity involved for simulating the power section behavior is such that it is very challenging to model everything involved. That is why we developed a new methodology in which we combine both modeling and experimental testing.

The entire methodology is summarized in the flowchart in Fig. 1. It is a high-fidelity model. The simulation requires material properties and geometry as input, along with the required operational parameters. 3D stator profile scanning is one of the most effective methods for obtaining the real geometry. Theoretical "drawings" for rotor and stator profiles can be used instead; however, this may reduce the simulation accuracy, especially for failure analysis.

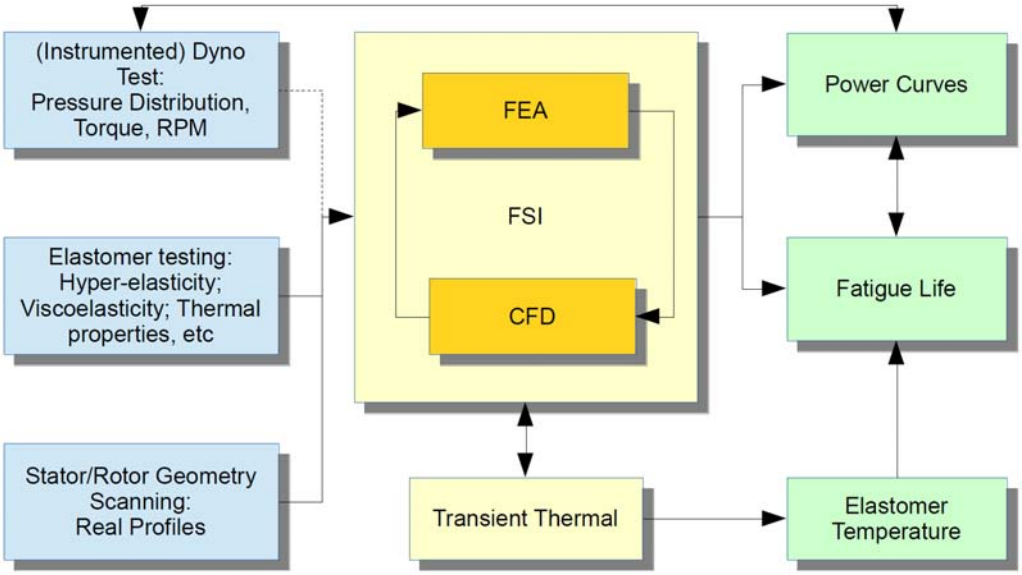

Figure 1—Flowchart showing the workflow for the methodology combining testing and modeling

Elastomer testing should be performed in different aspects: hyperelastic and viscoelastic properties, thermal capacity and conductivity, and the mud compatibility effect. As the practice shows, all these factors are significant and their relative importance will depend on the cases considered; that is why it is essential for the model to incorporate them all.

Usually for testing power sections, a functional test called dynamometer testing is performed. It consists of putting a power section inside a flow loop driven by one or two pumps and applying a restriction force at the end with clutches or brakes. For the modeling, an instrumented dynamometer test (IDT) can be used as the source of input data for the simulation through its capability to give pressure and temperature distribution along the power section length, but, more importantly, it serves as a powerful verification tool.

All these inputs are used in an FSI model, which is a combination of FEA and CFD techniques. The FSI model is coupled with thermal transient simulation, which predicts the elastomer temperature—one of the model outputs. The fatigue life is predicted based on elastomer loading history and temperature/mud effect. Power curves are built based on both FEA/CFD and can be easily validated by running a dynamometer test.

A more detailed description of the components of the methodology—instrumented testing; elastomer testing; stator geometry scanning; FEA, CFD, and FSI; thermal; and fatigue modeling—is given in the following sections.

Instrumented Dynamometer Testing. One important aspect of the experimental testing is the instrumented dynamometer test (IDT). It consists of putting different sensors along the power section, such as pressure sensors, temperature sensors, displacement sensors, and flow sensors to name a few; the goal is to try to accurately capture the kinematics and the kinetics behavior of the power section and then input the characterized kinetics inside the modeling scheme. By doing so, we can precisely understand the pressure and temperature profile of the power section and, using the model, derive their effects on the power generation and the stress fatigue. Fig. 2 shows a picture from the IDT setup on a dynamometer. Sensors are placed at various locations and their outputs are synchronized.

Figure 2—IDT with different sensors placed on the power section.

The basic kinematics of the power section is well known:

- The rotor has one lobe less than the stator.
- The rotor performs a planetary motion: it rotates around its own axis, which simultaneously circumscribes a circular orbit around the fixed stator axis.

Fig. 3 depicts an example of the motion of the rotor. Despite these simple principles, the kinematics of the power section is quite complex (Aage et al. 2006). The motion of the rotor is induced by the combination of the fluid velocity and the pressure differences between adjacent cavities. Cavities denote volumetric sections of fluid, which are trapped in between the contact lines between the rotor and the stator. These contact lines are called sealing lines. Each of the cavities separated by the sealing lines will have different pressure values. In reality, these cavities inside the power section progress in a spiral motion both axially and rotationally at the same time. This process gives these systems the names progressive cavity pumps or positive displacement motor. It might be challenging to uncover the pressure values on each cavity and the relationship between these values and the overall behavior of the power section. Often, one must first describe the mathematics/geometry of these cavities through a detailed kinematics analysis.

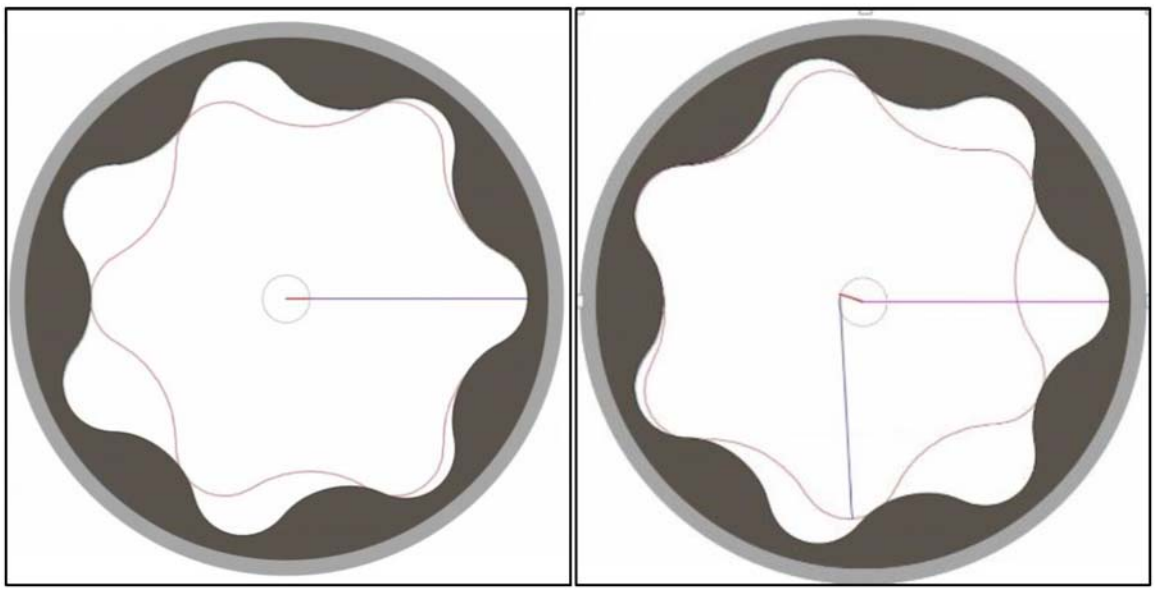

Figure 3—Basic kinematics of the rotor motion inside the stator.

Fig. 4 shows a typical cavity map of a 4/5 power section viewed from the rotor. The lines represent sealing lines, and the colored parts depict the cavity surfaces on the rotor. These cavities and sealing lines will move as the rotor moves, and the description of these motions are the main goal of the power section kinematics analysis.

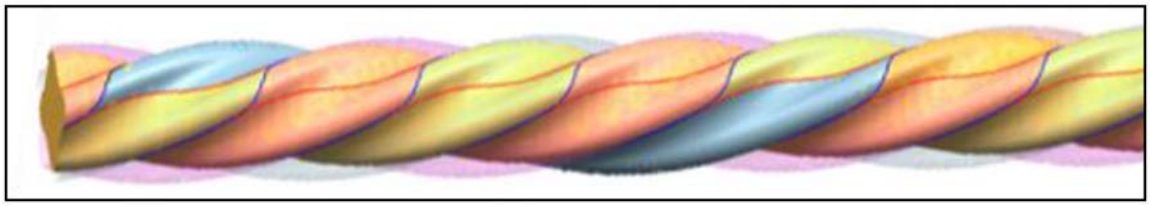

Figure 4—Contact lines on the rotor (stator is not shown; cavities are semitransparent).

Upon completing the kinematics description, one can derive the pressure and temperature mapping of the power section via the instrumented dynamometer test. These pressure and temperature profiles will be used as part of the modeling methodology, as can be seen on the workflow (Fig. 1). They represent an essential part of the workflow since they provide the necessary inputs to the modeling scheme. For power sections not tested with the IDT, a CFD/FEA workflow was also tested. This workflow was validated using the tested power sections. An example of the validation is discussed on the section 3.4.

Elastomer Testing. Following the IDT, other important experimental tests include elastomer characterization testing. This testing involves a series of experimental tests to understand better the mechanical behavior of the rubber. Elastomers are highly nonlinear materials; hence, to model them, one needs to test them in many different areas. Below are examples of tests to be performed for elastomers prior to incorporating them inside a model:

- Hyperelastic properties. These generally include simple, planar, and equi-biaxial tension and volumetric compression, which are required for hyperelastic models. The material model can be improved by taking into account the Mullins effect (Diani et al. 2009) dynamic softening, and creep. It is very important to run these tests at different temperatures.
- Viscoelastic properties. Tests for viscoelastic properties usually involve the measurement of loss/storage modulus at different conditions of temperature, frequency, and strain/stress.
- Thermal properties. Thermal measurements include thermal expansion coefficient, thermal conductivity, and specific heat. These parameters are required to perform a transient thermal simulation. Thermal expansion is needed to predict change in fit at elevated temperatures.
- Fatigue properties. Fatigue properties are used as one of the fatigue models applied to FEA solutions, and the testing includes determination of crack growth rate under different conditions and initial flaw size (see section 2.6).
- Mud effect. Mud effect is the characterization of changes in the elastomer properties induced by mud impregnation. Optionally, all the properties above can be remeasured after mud immersion. However, in general, swell and stiffness change due to the mud impregnation are required. In many cases, the motor run time is less than the time required for the mud to ultimately soak the elastomer; thus, the diffusion coefficients of some mud components may be required as well. We will come back to that in the next section, under "Mud." (3.3.5)

Out of all these tests, the most critical one is the hyperelastic characterization test. Elastomers are hyperelastic, which means that their strain energy density functions have different forms. The commonly available strain energy functions *(W)* for elastomers are represented generally in terms of strain invariants:

$$I_1 = \lambda_1^2 + \lambda_2^2 + \lambda_3^2, \qquad I_2 = \lambda_1^2\lambda_2^2 + \lambda_2^2\lambda_3^2 + \lambda_1^2\lambda_3^2, \qquad I_3 = \lambda_1^2\lambda_2^2\lambda_3^2,$$

where λ represents the elongation in one particular direction.

Using these strain invariants, one can choose one particular model among a long list of available models to express the strain energy density. Examples of models include neo-Hookean model, Ogden, Mooney-Rivlin, and Arruba-Boyce. One can also use a generalized form (Bower 2012), such as

$$W = \sum_{i=1}^{N}\sum_{j=1}^{N} C_{ij}(\overline{I}_1 - 3)^i\,(\overline{I}_2 - 3)^j + \sum_{i=1}^{N}\frac{K_i}{2}\left(\sqrt{I_3} - 1\right)^2$$

where C_{ij} and K_i are material properties that can be derived from experimental testing.

In reality, the choice of the model and the resulting characterization testing are critical in the overall scheme. That is why one needs to evaluate first typical strain levels to consider for the chosen elastomers.

Stator geometry scanning. Any approach to model any PCP/PDM mechanism requires stator/rotor geometry as the input parameters for either FEA, CFD, or FSI calculations. Traditionally, that geometry is defined by 2D curves or 3D surfaces built on the set of discrete points. Typically, this approach works for designing power section from scratch and the defined stator/rotor shape is considered as a nominal (targeting) geometry. However, due to many factors, such as manufacturing tolerances and imperfections, rotor/stator wear, elastomer swelling, uneven thermal expansion, etc., the real geometries of both stator and rotor might seriously deviate from the nominal values.

The novelty of our approach is the possibility to utilize the actual shape of both stator and rotor in the modeling strategy when needed. Two independent methodologies to capture the geometry of any power section were established, one for the rotor and one for the stator.

The rotor geometry can be extracted by either a coordinate-measuring machine (CMM measurement) or 3D optical image mapping. Although there are a few challenges in extracting the rotor geometry, both methodologies are well known. In contrast, extracting the stator geometry is a complex and non-ordinary task. To solve it, we implemented a comprehensive and innovative technology known as 3D laser mapping (or laser scanning).

This technology is based on the optical triangulation approach. The laser beam comes from the sensor head and hits the target surface. Reflected light is captured by a special lens, and ultimately it becomes focused on a special photodetector. Changing the distance between the laser source and the target surface will move the imaged spot on a photodetector matrix.

Optical triangulation is shown in Fig. 5.

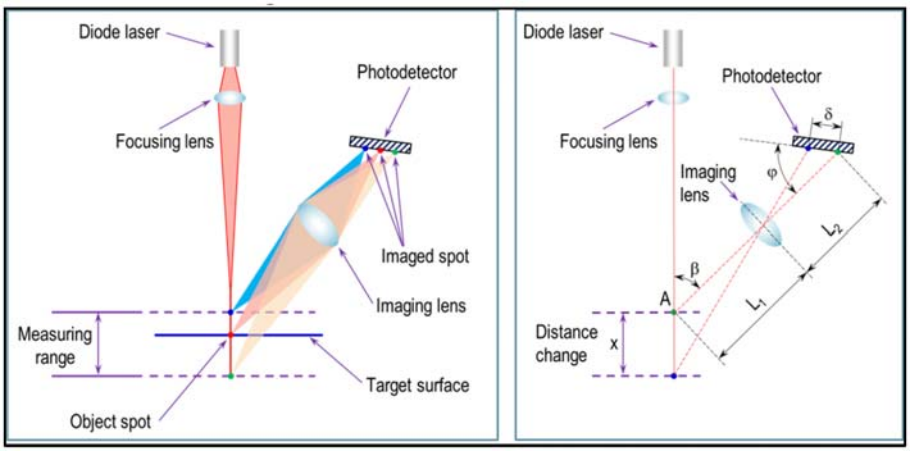

Figure 5—Optical triangulation (generic scheme).

The distance X might be defined as $X = \frac{L_1 * \delta * \sin\varphi}{L_2 * \sin\beta - \delta * \sin(\varphi+\beta)}$

In this formula

- X is the distance to measure.
- δ is the distance between corresponding image spots on photodetector.
- β is the angle between the laser beam and the axis of the imaging lens.
- ϕ is the angle between the surface of photodetector and the axis of imaging lens.
- L_1 is the distance between point A and the center of imaging lens.
- L_2 is the distance between the center of imaging lens and the image spot on a photodetector.

Thus, by analyzing the position change of imaged spot on the photodetector, it becomes possible to judge what the actual distance between the laser source and the target surface is.

In Fig. 6, a real sensor is shown, and one can see how it works inside the stator.

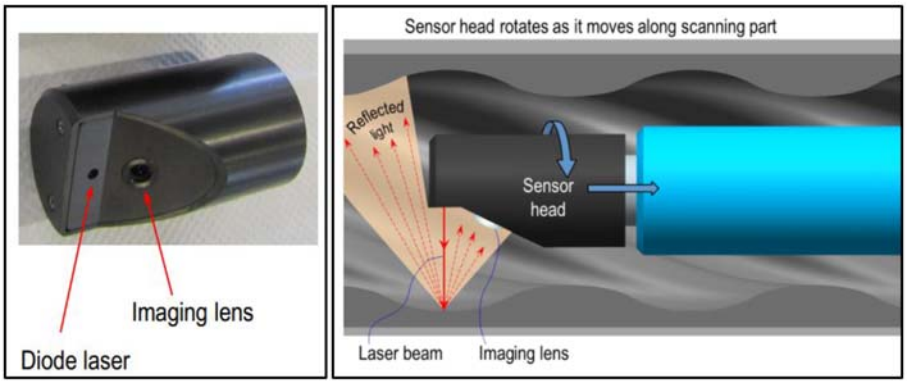

Figure 6—Real sensor and measuring scheme.

We put a sensor inside the stator and pull it along the length. The sensor head continuously rotates and scans the inside surface. Simultaneously, a special linear encoder captures the axial coordinate. The equipment we have can also measure the straightness of the internal rubber lining with an added device. A special processor combines all profile and straightness measuring data into a 3D map, which can be imported to an FEA/CFD/FSI software package for further calculations. The example of scanned stator surface is displayed in Fig. 7.

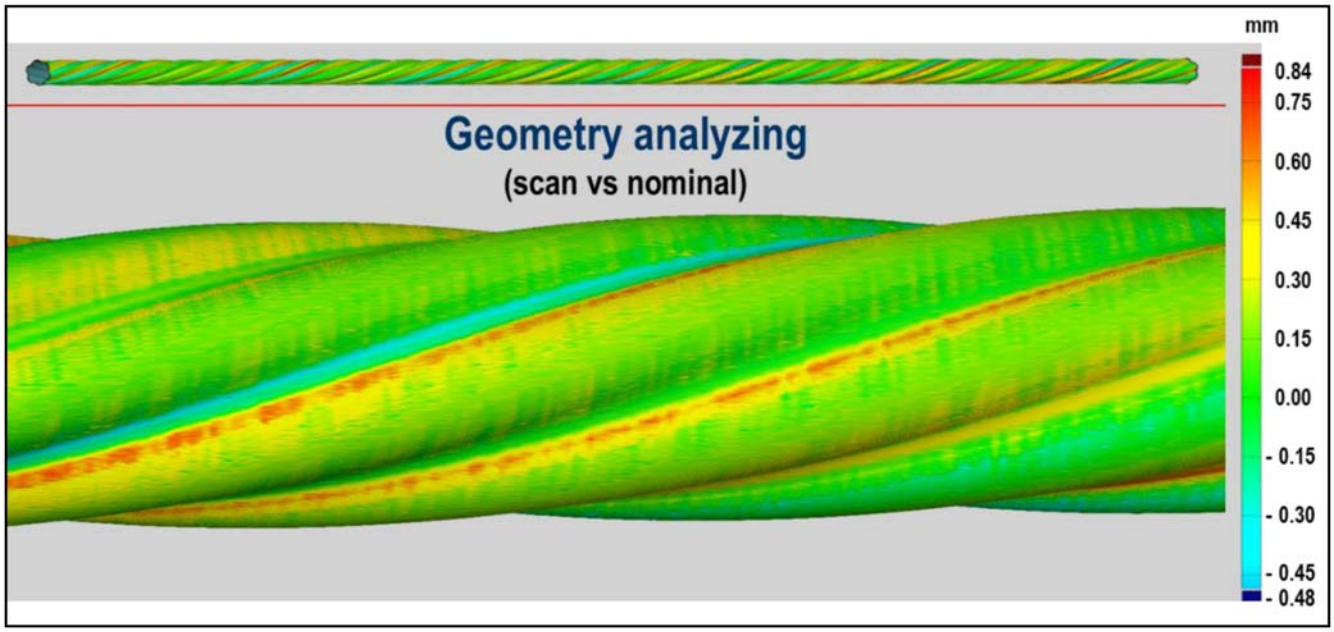

Figure 7—3D scanned stator surface vs. nominal geometry.

Despite its complexity and its seemingly excessive information, 3D laser scanning is one of the essential tools in power section modeling. Ultimately, it helps us to identify (just to name a few)

- The effect of manufacturing tolerances on power section performance and reliability
- The effect of wear on power section performance and reliability
- The power section performance in nonstandard environment/conditions (interference fit out of tolerance (see section 3.3.3), rubber permanent deformation, variable fit along the length, etc.)

FEA, CFD, and FSI. Another vital aspect of the methodology is the FSI scheme. The methodology uses inputs from the pressure and temperature profiles, the elastomer characterization, the 3D mapping, and/or the kinematics design into a FSI scheme. FEA and CFD have been combined together to iteratively solve the stress and deformation on the stator and rotor and the flow through the cavities. The effects of the FSI on the motor performance and reliability are included in the simulations by exchanging the pressures and deformed geometries at the stator and rotor surfaces.

A commercial FEA tool has been embedded into a custom simulation platform to simulate the mechanical performance of the power section. Both the mechanical load and pressures on the stator and rotor surfaces are included for modeling the stress and deformation. The deformed stator and rotor geometry were used as physical boundaries of the fluid domain and transferred to a fluid meshing tool, which is very good at surface geometry handling.

As seen in Fig. 8a, cavities are formed between the stator and rotor surfaces whereas there is no fluid in the region where full contact is formed. The whole length of the tool is modeled with a flow entrance and exit region. Due to limitation of page sizes, only a portion of the domain is actually shown here. Fig. 8b shows a typical generated computational mesh for the corresponding region. The entire tool is meshed and modeled such that the cavity geometry and sealing could be quite different depending on its operating and local conditions. Flow simulations are carried out using a commercially available fluid solver as the numerical solver for the steady-state Reynolds-averaged Navier-Stokes equations. Once a converged solution is obtained, the pressures in the cavities are put back into the FEA setup to solve again the solid stress and deformations. These steps are progressed iteratively until a converged solution for both the FEA and CFD is reached. Depending on the geometry and flow parameters, an under-relaxation factor

could be applied for better convergence. In this particular example, the fluid is water, which is treated as incompressible and has a density of 1000 kg/m^3 and viscosity of 0.001 kg/m-s. The standard k-ε model (Wilcox 1998) with the standard wall functions is selected to model the turbulence efficiently.

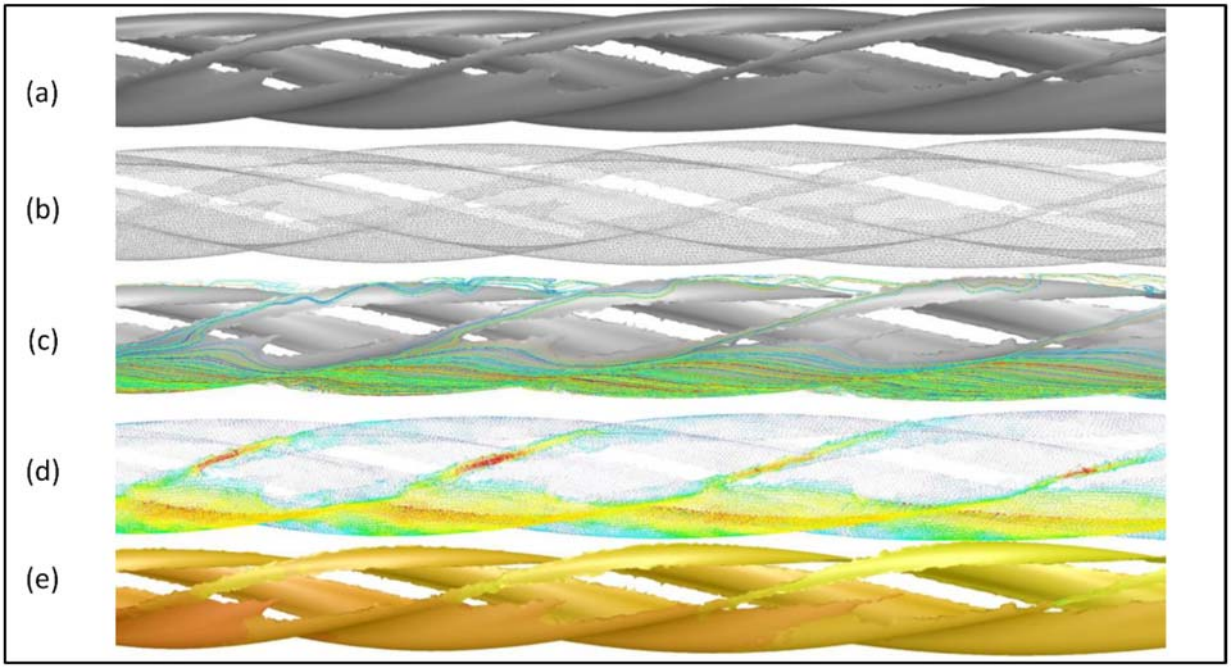

Figure 8—(a) Cavity geometries formed by the deformed rotor and stator. (b) Computational mesh generated. (c) Flow path lines through the cavities. (d) Flow velocity vectors right above the stator surface. (e) Fluid pressures on the stator surface.

Thermal. Despite the seemingly comprehensive methodology described above, the complete model requires additional efforts. In reality, not only is the elastomer a highly nonlinear material, but it also experiences hysteresis heating. This means that when we constantly load and unload the elastomer, it follows different paths from down to up compared to from up to down; the difference between the two paths is the energy generated through heating. In other words, all elastomers show so-called viscoelastic behavior (i.e., they behave as elastic bodies and liquids at the same time). The viscous part of the response is not recovered as deformation energy, and thus reduces the efficiency of the power section; more importantly, it leads to heat buildup inside the rubber lobes.

As the result of FSI simulation, the deformation $\varepsilon(t)$ is obtained for each element as the function of time within the loading cycle $t = 0 \ldots T$. The viscoelastic behavior is defined by the ratio between the viscous and the elastic response - $tan\ \delta$ (Lakes and Quackenbush 1996), which may depend on frequency, strain, temperature, etc. In this case, the stress $\sigma(t)$ as a function of time can be computed. By plotting the stress and the strain as parametric functions, a closed hysteresis loop can be obtained, as shown in Fig. 9.

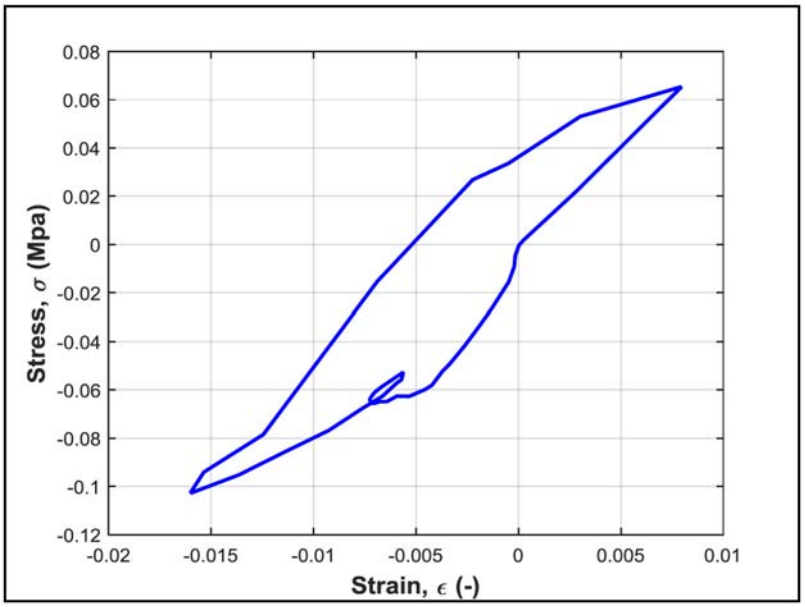

Figure 9—Stress-strain curve of an elastomer showing closed hysteresis loop.

The area inside the hysteresis loop is the dissipated energy density during one cycle or the amount of energy transformed into heat during one cycle. It might be expressed as $E = \int_0^T \sigma \varepsilon_t' dt$ and the volumetric heat flux $q_v = E/T$. The temperature in the rubber lobe now can be found by solving the heat equation:

$$\rho c_p \frac{\partial \theta}{\partial t} - \nabla \cdot (k \Delta \theta) = q_v,$$

Where ρ is density, c_p is specific heat capacity, k is thermal conductivity, and θ is temperature inside the elastomer.

Note that for determining θ, the mud temperature is used as initial condition and so are the boundary conditions at the contact between the mud and the elastomer.

It is obvious that the heat buildup due to the viscous energy dissipation is proportional to the loading frequency, which can be found as the product of the motor rotation speed and the number of rotor lobes. It may also be shown that the heat generation increases with the *tan δ* and deformation values.

Heat buildup makes the problem more complex by causing the rubber temperature to increase. It affects both tan δ and the deformation level mainly via the thermal expansion of the rubber, but some changes in stiffness are possible as well. To overcome this issue, the transient thermal equation and FEA/FSI problem are solved simultaneously doing several time iterations to address the changes in heat generation, geometry, and material properties.

Fatigue Modeling. When trying to model fatigue behavior of mechanical components, we often have to deal with crack initiations and crack propagations. In terms of elastomer materials, when we subject them to deformation and cyclic loading they sometimes break. We can try to estimate the breaking strain and stress based on the stress required to break all chemical bonds in one plane, but doing that we get breaking stress much higher than real test results. The reason for that is the existence of small cracks called flaws in any elastomer.

This means that when modeling elastomer fatigue, the main thing to consider is crack propagation from small existing cracks. If we do many cycles of loading, the crack length increases during each cycle until reaching a macroscopic size. Therefore, under cyclic loading, eventually, we will get the material broken, even if the load is below the break stress limit.

This process is so called fatigue and the number of cycle to break the material is called fatigue life. The main output from the fatigue modeling will be the fatigue life estimation.

Fig. 10 is an example of a power section, which failed after certain hours of drilling due to fatigue. One can clearly see the cracking on the rubber surface. To avoid such catastrophic power section failure downhole, accurate prediction of fatigue life is very important.

Figure 10—Example of failed stator due to fatigue.

Results and Application

Power Prediction. When evaluating the performance of a motor power section, it is, in general, necessary to refer to power curves. These indicate the RPM and torque output of the mud motor depending on the flow rate and differential pressure during operation.

Power curves are very important modeling output, since the information determines the motor usability. The power curves show the dependence between torque, RPM, flow rate, and pressure through the motor. As stated before, modeling these parameters is challenging because it includes interaction between the rotor, the stator, the elastomer, and the fluid. The general case can be solved as FSI, a combination of FEA and CFD, as explained in section 2.4. However, the FSI takes a significant amount of computation time. For simply deriving the power curves, one can use some simplified methodology. At the same time that we developed the FSI, we also constructed a simplified model to compute power curves with the results available within 1 hr and often less than that. The methodology utilizes a simplified leakage algorithm instead of simulating the full 3D interaction between the fluid and the solid surfaces of the rotor and the stator. The model can take into account temperature, elastomer properties, and the exact rotor/stator geometry. It matches reasonably well with the dynamometer test results as can be seen from Fig. 11.

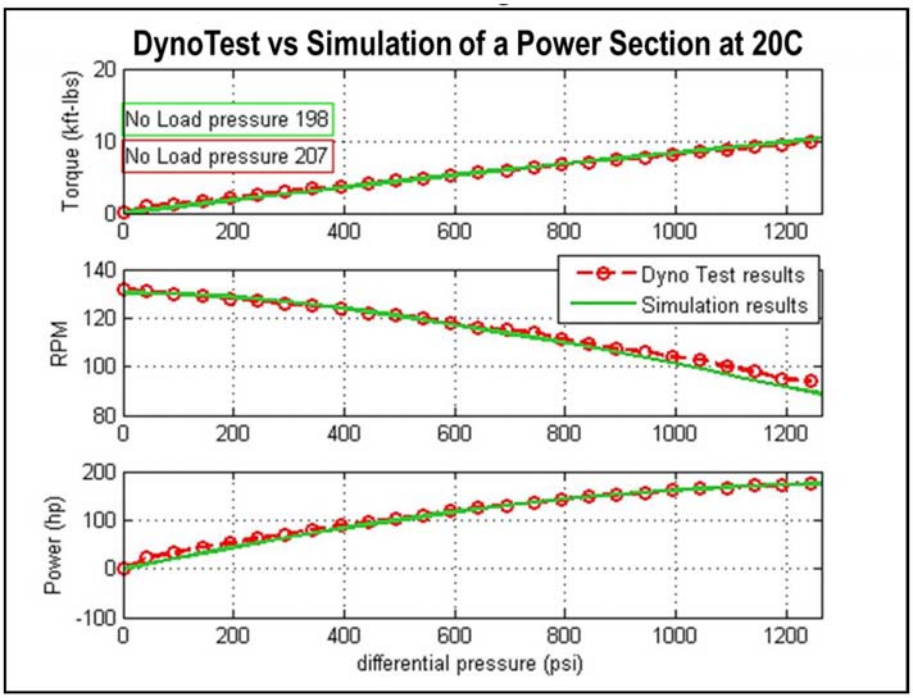

Figure 11—Power curve simulation vs. dynamometer test.

In Fig. 12, one can see the graphs for the power prediction for three elastomers E1, E2, and E3. They are known to deliver different power when used in motors because of the different stiffness. The model perfectly tracks that. The rubber stiffness affects not only the RPM curve behavior, but also the torque slope at high differential pressure due to the lobe deformation and increased viscous and friction losses.

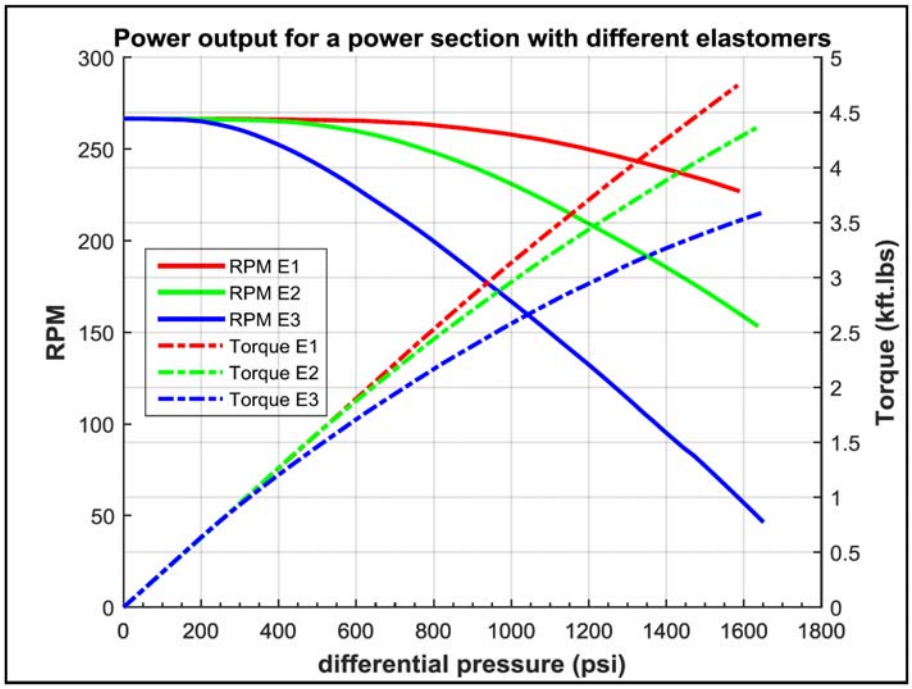

Figure 12—Power curve prediction with three different elastomers.

The power prediction is also very important for further reliability modeling because its data are used for transforming operational parameters (differential pressure, flow rate, and torque) into boundary conditions for FEA/FSI and fatigue modeling.

In addition, it is fair to mention that using the overall modeling capability, we have run many sensitivity analyses to understand how to optimize the power generation and the run life under different conditions. In particular, we ran simulation with different flow rates, different temperatures, different interference fits, different mud types, different profiles, and different types of power sections… We will discuss some of these results in section 3.3 related to the sensitivity analysis.

Fatigue Prediction. As stated previously, the fatigue life prediction allows the user to understand how long the power section can be loaded before the elastomer starts failing. It indicates the estimated durability of mud motor power sections. Fig. 13 shows a comparative study between a failed stator on the right and the modeled predicted fatigue failure. The right part of the figure depicts the bottom part of a thin-wall power section. It may look like a conventional power section but it is a thin-wall with the rubber cut back at the end of the stator. Turning to the left side of the figure, the red color represents the areas of low fatigue life or where the rubber has high risk of fatigue failures whereas the blue colors are for long-life areas. Looking carefully at the figure, one can spot short black bars; these indicate the most probable crack directions. If one looks anywhere besides the flank area of the stator, one can see that the crack directions are positioned randomly, suggesting that in those areas there are no particular preferred crack directions. However, at the flank, one can appreciate that almost all cracks are perfectly aligned and extend more deeply into the rubber. This suggests that for this particular power section, the cracks will penetrate deeper inside the rubber before chunking occurs. One can observe the exact same phenomenon in the picture on the right. The fatigue life prediction is found to be extremely close to reality. The model predicts not only the lifetime of the stator under the run conditions appropriately with error margin within the 30% range (which is rare in fatigue prediction), but also the location of the cracks and direction of propagation of the cracks with extremely high accuracy.

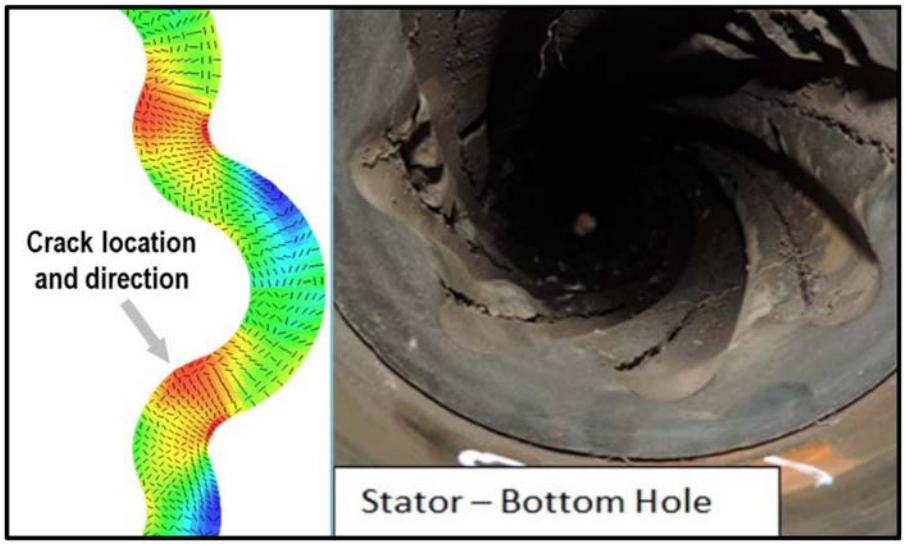

Figure 13—Comparison between fatigue prediction model and real stator fatigue failure.

Furthermore, the fatigue modeling allows understanding better the optimized operational parameters such as differential pressure or flow rate to be used for running the motor in particular applications. One can find more information on effects of operational parameters on the fatigue life prediction in section 3.3.1.the next section. In the meantime, Fig. 14 is an example of the fatigue life prediction of a power section subjected to

varying differential pressures with the same mud but under different temperatures. Note that the fatigue life is plotted in log scale. The power section has a slightly better performance in fatigue life when subjected to the lower temperature of 90 °C compared to 100°C.

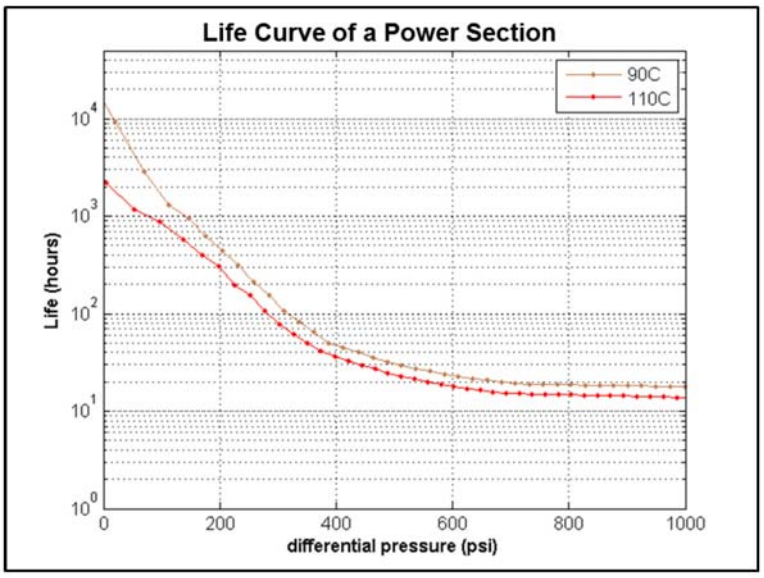

Figure 14—Fatigue life prediction of the same power section at two different temperatures.

Sensitivities.

Operational Parameters

Operational parameters such as drilling differential pressure and flow rate can significantly affect the power generation and the fatigue life of the mud motor. Fig. 15 depicts the comparative study of the same power section using the same elastomer at the same flow rate with different differential pressure. The estimated power output is found to be 220 HP if drilling at 800 psi. If one drops the differential pressure to 600 psi, the power output is 180 HP, which represents only 18% of power decrease. In contrast, moving from 800 psi to 600 psi, the differential pressure will increase the fatigue life by 2.5 times. In reality, the decrease in power output would have only a minor effect on the drop of rate of penetration (ROP) but would have an order-of-magnitude effect on the reliability.

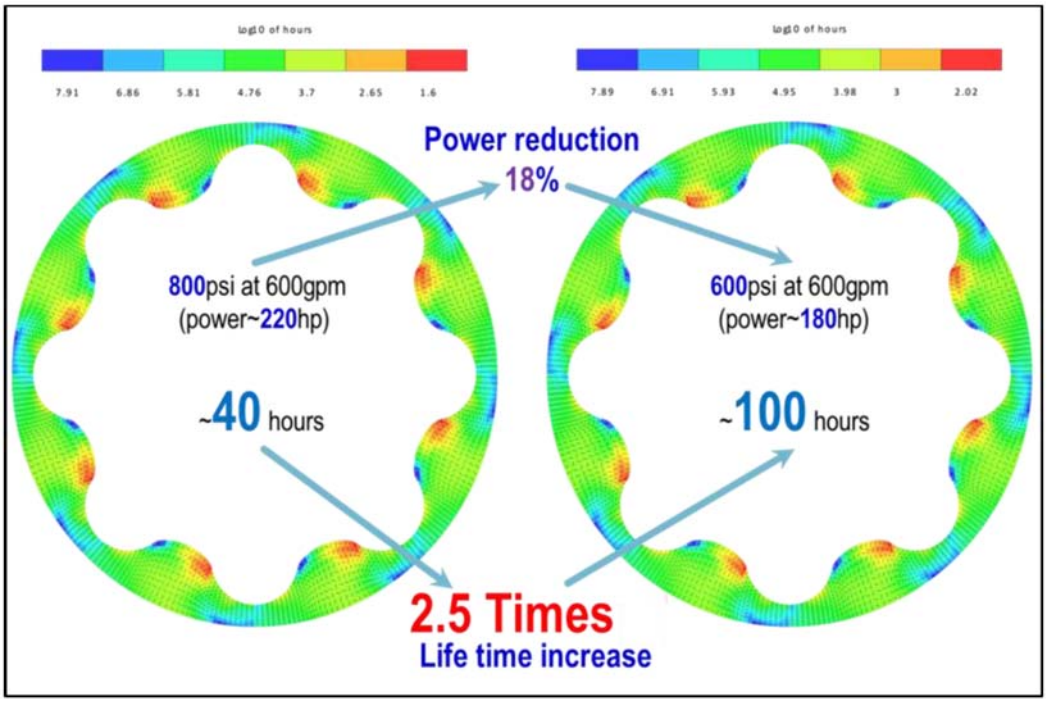

Figure 15—Sensitivity to differential pressure.

Fig. 16 illustrates the influence of the flow rate on fatigue life prediction on a 9 $^{5}/_{8}$-in. power section in the same mud and temperature, whereas Fig. 17 shows the power output at the same conditions, and Fig. 18 illustrates the effect of hysteresis heating. As one can expect, the power section has slightly better performance in terms of fatigue life when subject to lower flow rate compared to higher flow rate. This analysis, along with the power generation and the hysteresis heating can help us select an optimum flow rate for particular running conditions and field requirements.

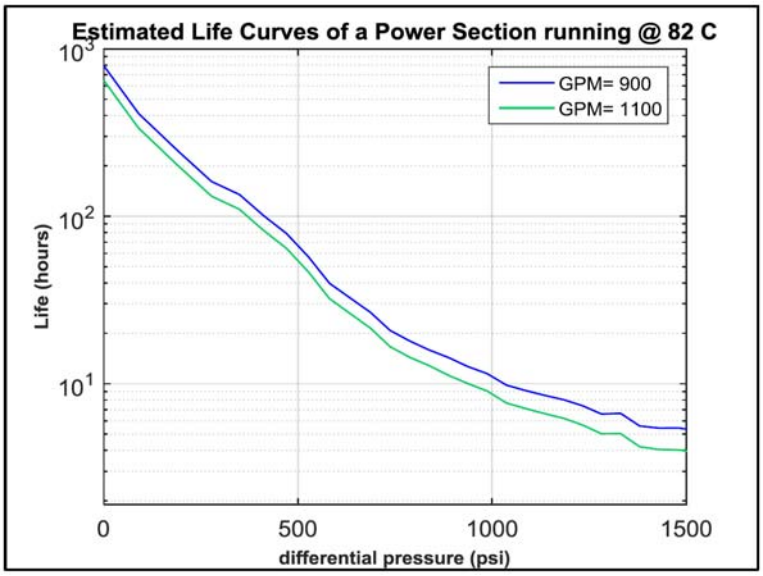

Figure 16—Effect of flow rate on fatigue life of power sections.

As stated before, Fig. 17 presents the influences of the flow rate on the power curve prediction under the same temperature. One can see that higher flow rate introduces higher RPM in an obvious way. The

black dotted line represents the torque of the power section. It was confirmed that torque versus differential pressure does not change dramatically with mud flow rate since the torque is a direct function of the pressure difference between cavities. These curves at different flow rate can serve as a powerful guideline to avoid rotor stall in downhole operating conditions, as different flow rate will result in different stall pressure.

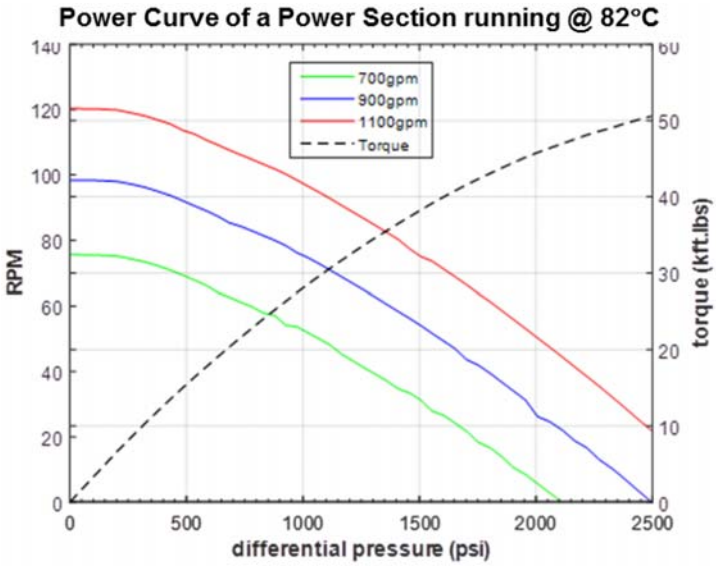

Figure 17—Effect of flow rate on power generation of a 962-in. motor.

Besides that, flow rate will affect also the temperature buildup inside the rubber due to the hysteresis heating effect. In Fig. 18, the higher flow rate (1100 gpm) leads to a rubber temperature runaway phenomenon that will be discussed more on section 3.3.2. The simulation enables us to understand better how to run this power section. In particular, it is better to run it at lower flow rate or change the interference fit (to be discussed on the section 3.3.3) to avoid possible rubber chunking failure due to high temperature.

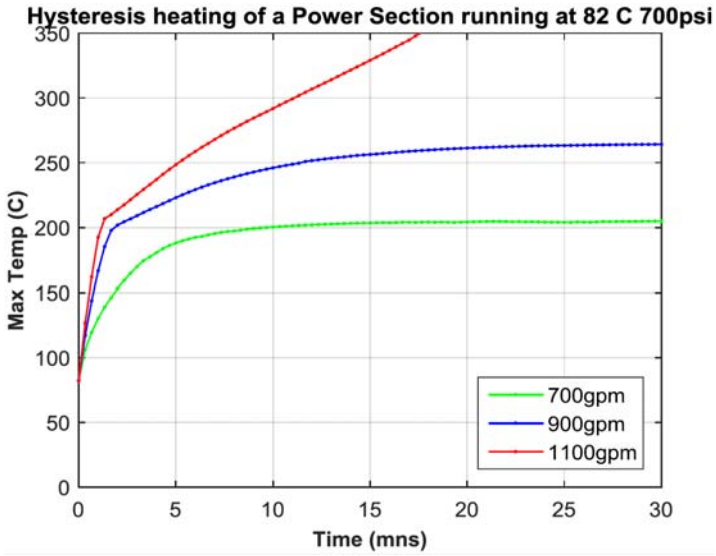

Figure 18—Effect of flow rate on hysteresis heating inside a stator.

Now, one can certainly see how we can tie up the operational parameters effects with the monitoring system to deliver a higher shoe-to-shoe ROP. Obviously, these parameter effects will be very useful during

the planning phase for defining their range of utilization but, more importantly, one can use the modeling capability to derive optimized real-time drilling parameters by adjusting on the fly the flow rate and differential pressure depending on the current ROP, the temperature, and the estimated cumulative fatigue life. This may significantly improve the drilling operations.

Flow and Heating

Hysteresis heat buildup can be very damaging to a stator. Under certain conditions, a positive feedback or runaway effect can be formed between the heat generation and the temperature through thermal expansion. In Fig. 18 it is shown how it may happen with a power section. The mechanism behind the runaway effect is depicted below:

- First, the load is very high, which leads to higher strain energy.
- From this high strain energy arises higher energy dissipation through heating.
- The heat generated inside the rubber induces higher thermal expansion of the rubber.
- The higher rubber expansion generates tighter interference fit.
- The tighter interference fit (see 3.3.3) induces higher contact pressure from the rotor to the stator, which increases the load, and the phenomena cycle from there until a very high temperature occurs, which can result to an outburst inside the rubber (see Fig. 19).

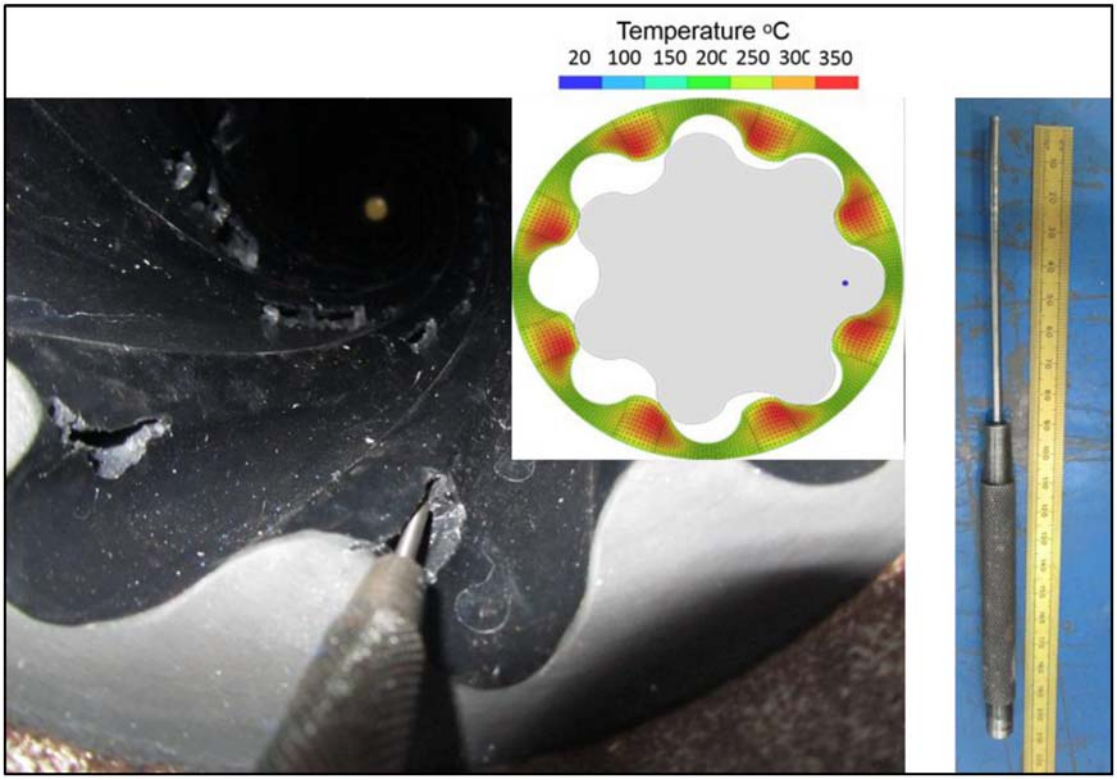

Figure 19—Picture of a stator damage due to heat runaway effect.

On the low flow rate level (700 or 900 gal/min), the maximum rubber temperature stabilizes on some level, and the temperature increase is roughly proportional to the flow. After increasing the flow rate to around 1100 gal/min, the temperature never stabilizes fully because of the positive feedback that is established between heat buildup and temperature. This temperature runaway may lead to rapid, immediate stator failure. Excessive flow rate is one cause of temperature runaway, but other factors such as the interference fit and differential pressure, can activate the same problem. When running mud motors, it

is critical to find the right balance between the interference fit, the load (differential pressure), and the temperature inside the rubber.

Interference Fit

As mentioned above, an important geometrical factor affecting the reliability and performance of the mud motor is the motor interference fit or simply motor fit. The definition of this parameter is relatively simple:

$$\textbf{Fit} = \textbf{Rotor Mean Diameter} - \textbf{Stator Minor Diameter}$$

Selecting the right fit can be critical for operating mud motors properly. There are numerous recommendations and guidance on how to choose the right fit. However, most of current recommendations (at least publically available) are very generic. In most cases, they are related on one way or another to evaluating fit changes with respect to operational temperature increase or decrease via the use of the coefficient of thermal expansion (CTE) of the stator elastomer. Each rubber has a certain tendency to expand as the temperature increases, so by correlating the expansion of the rubber under particular temperature with the desired fitting of the rotor inside the stator, one can predict the nominal value of the fit to be used.

Besides the CTE, many other factors affect the estimation of the interference fit such as the swell from the elastomer-mud compatibility, the changes in rubber mechanical properties at different temperatures, or even the rotor/stator profile distortions downhole compare to the original profile.

The exposed approach is to use an unbiased modeling capability to understand how the fit affects the behavior of power section first.

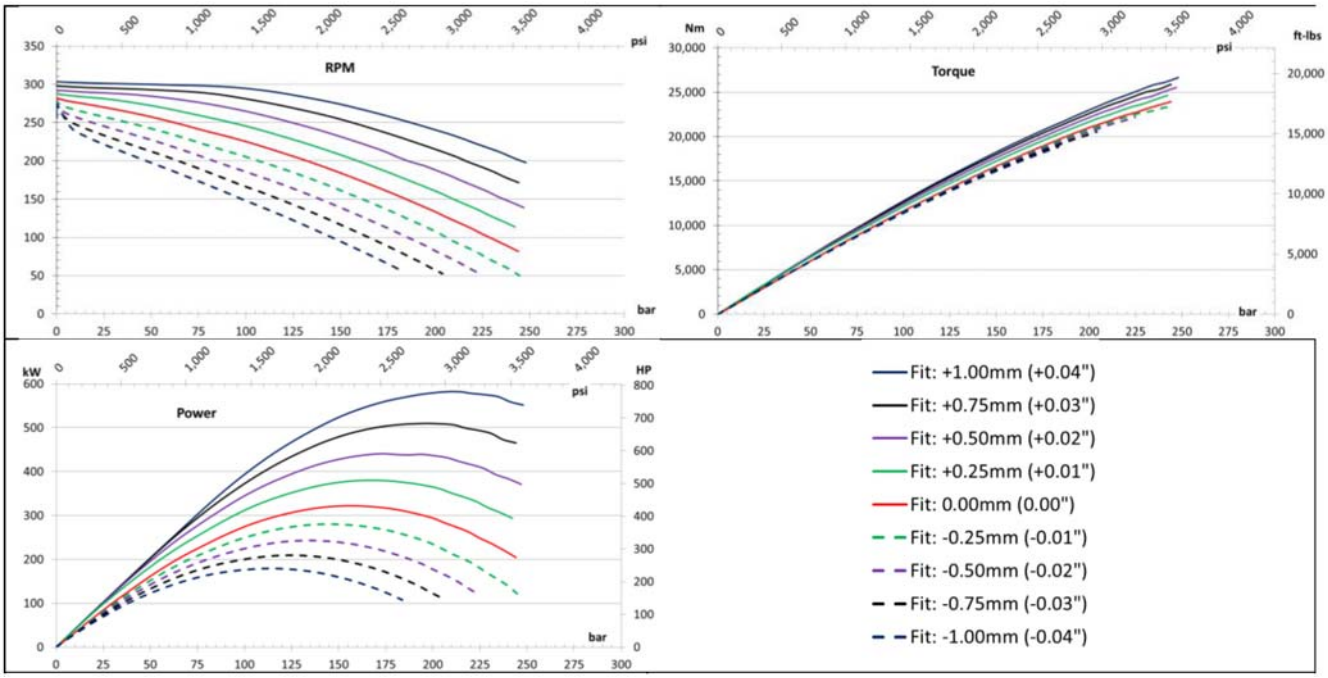

Fig. 20 demonstrates the impact of the motor fit on the power generation of a 675-in. mud motor. Fit increment was chosen as 0.25 mm (0.010 in.). All curves are simulated for the flow rate 38 l/s (600 gal/min) and 20°C (68°F) ambient temperature.

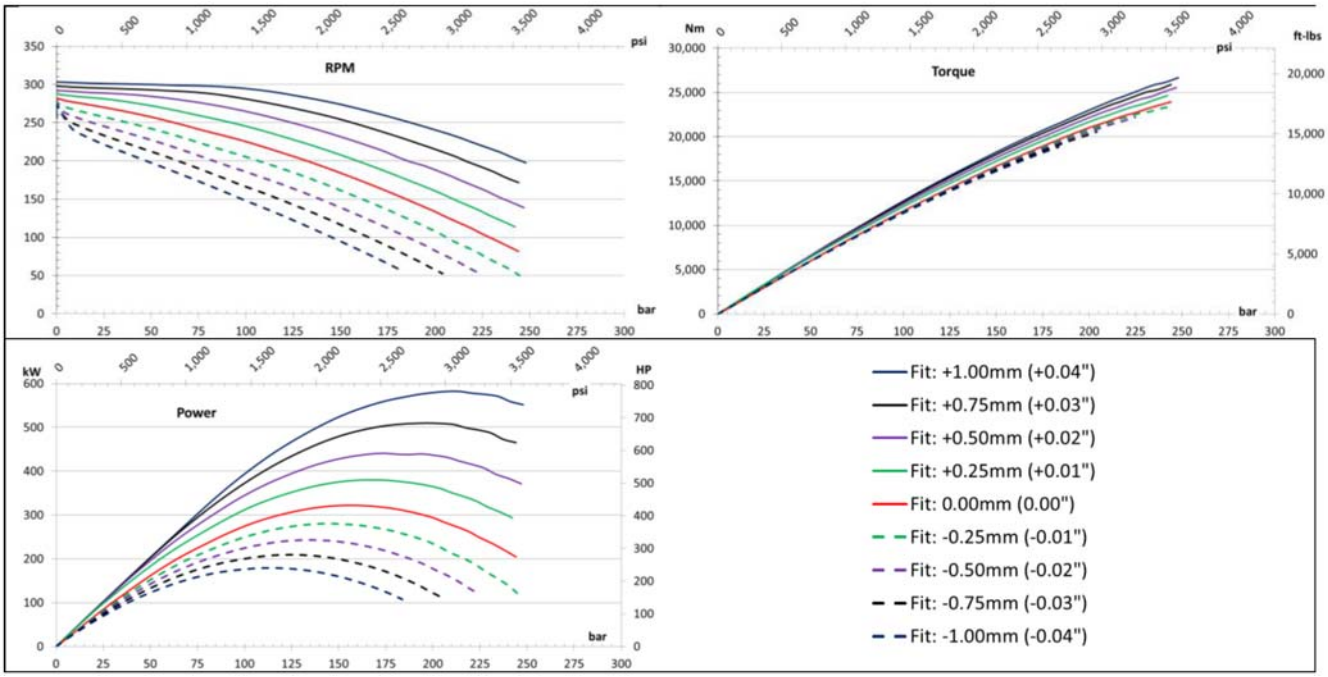

Figure 20—Modeled motor behavior with different fit.

As expected, a higher fit provides better performance through mainly the enhanced RPM capability.

In parallel to the performance evaluation, one can see how the motor fit affects the stator hysteresis heating. The influence of the motor fit on the hysteresis heating is very significant. In particular, when the fit is too tight and the operating temperature is too high, there is a high risk of temperature runaway effect as presented in section 3.3.2 (Fig. 21).

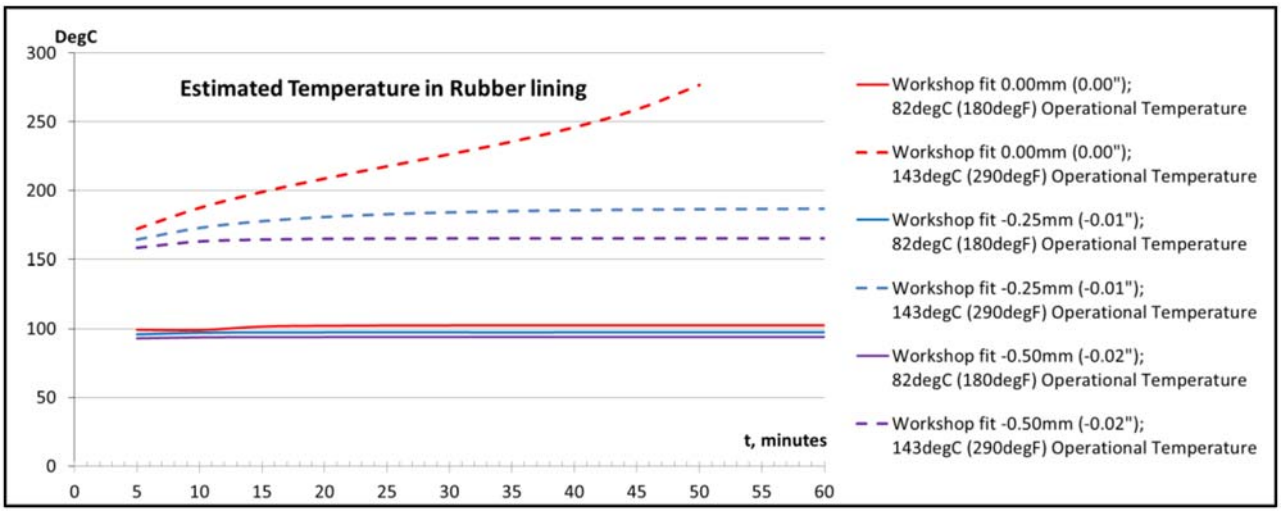

Figure 21—Impact of motor fit on the stator temperature buildup.

In summary, although a tighter fit will provide better power capability, it could also lead to rapid downhole failure. That is why estimating the right fit is so important if one wants to have an optimized shoe-to-shoe ROP.

The measurement of the fit is in general overly simplified. The common practice is to measure both rotor mean and stator minor diameters in a few cross sections along the length, then average the results. The main

benefits of this method are its simplicity, practicability, and effectiveness. However, it has many limitations; the weakest point is that it does not take into account the true stator/rotor geometry.

In contrast, Fig. 22 depicts the measurement of the stator diameter deviation made by the 3D laser scanning for the entire power section length. The diameter deviation band is approximately 0.4 mm (0.016 in.). That much difference in fit can lead up to 30% power reduction if considered uniform along the length according to the simulation on Fig. 20.

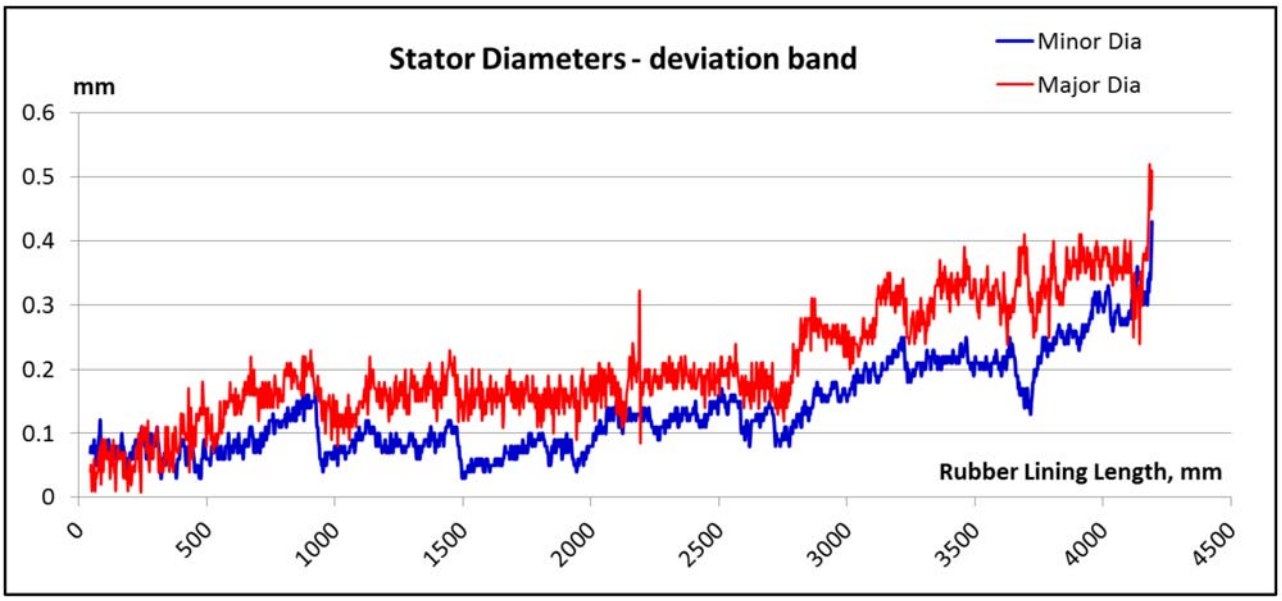

Figure 22—Deviation in stator minor and major diameters.

The case study below depicts a performance and reliability comparison between a used rotor/stator versus a new rotor/stator. In this study, the same fit is used but with different combination of rotors and stators:

- A new rotor
- A rotor that has been rechromed several times with the lobe thicker than necessary but the mean diameter similar to a new rotor
- A new stator
- A used stator with slightly worn lobes (with the actual shape evaluated by laser scanning machine) but the same minor diameter as a new stator

Traditional measurement methods would say that all the stators/rotors are the same. Fig. 23 illustrates the results. On one hand, the combination of rechromed rotor with the new stator provides the highest power; however, it would generate the highest hysteresis heating and the shortest fatigue life. On the other hand, the combination of the new rotor and with the worn stator would have the lowest heat generation but the power output would be poor. The best-balanced configuration is the new rotor assembled with the new stator, as anticipated.

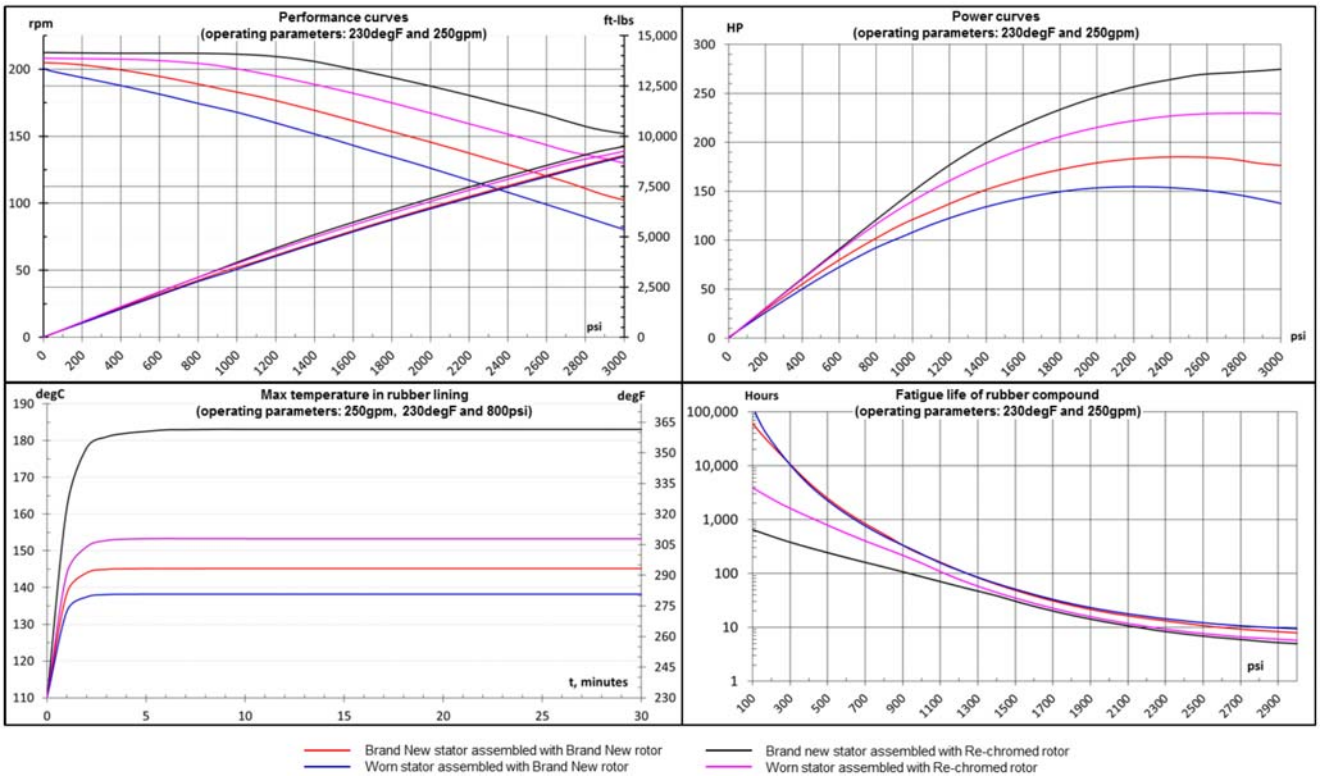

Figure 23—Performance of power section with the same fit but different stator/rotor shapes.

The main lesson from this study is that there might be significant differences between the assumed performance and reliability of a power section versus the actual ones, even if traditional measurements indicate that the power section is well within the specifications.

Elastomer

The predictive modeling enables understanding the behavior of particular elastomers in terms of fatigue resistance, hysteresis heating, and performance (power curve) well before releasing the elastomer or the designed power section. It allows a consistent analysis of the performance of different elastomers to select the best one for a particular application. This is a great opportunity to provide consistent performance with enhanced service quality.

In this particular section, we consider the effect of the elastomer on the performance and reliability of the power section. The performance aspect was discussed in section 3.1; one can refer to Fig. 12 for more details.

In terms of fatigue, one can see on Fig. 24 the fatigue life prediction of the same power section with the same interference fit run at the same flow rate but with two different elastomers.

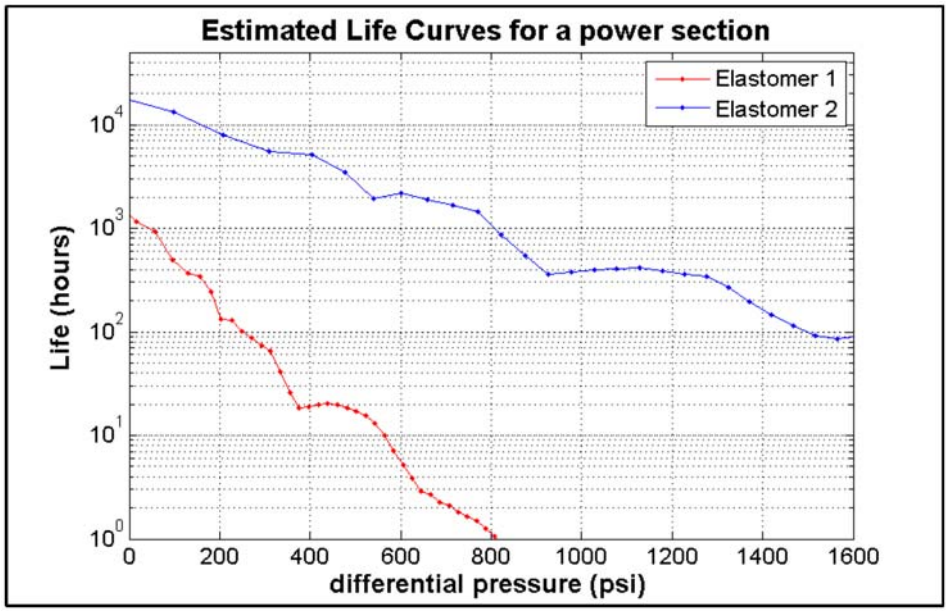

Figure 24—Fatigue life prediction of the same power section with two different elastomers.

Elastomer 1 shows significantly less life than elastomer 2 with the same load conditions. This highlights the strength of having such a modeling capability. In addition to the fatigue life prediction, both hysteresis heating and performance comparison can be achieved. Ultimately, when this information is combined with the mud information (see section 3.3.5), one can chose the best elastomer for the right power section in the right job to get the best performance and the highest reliability. The goal is to get the fastest shoe-to-shoe ROP.

Mud

Mud-elastomer interaction can significantly affect power section performance; this interaction is referred to as mud-elastomer compatibility. The mud effect on the elastomer can be divided into five categories:

- Profile change due to the rubber swell or shrinkage
- Changes in mechanical properties, generally softening or stiffening
- Changes in mechanical strength and fatigue life
- Profile changes due to erosion
- Profile and geometry changes due to different abrasion effect with different muds

The problem becomes more complex if we take into account the kinetics of the process. When an elastomer is exposed to mud, there is a diffusion process of some mud components into the elastomer and possibly the opposite process leaching of some elastomer components (plasticizers) to the mud. Mud diffusion into rubber makes it swell and often soften, and plasticizer leaching leads to the shrinkage and often to hardening. The diffusion process is described by Fick's equation (Fick 1855):

$$\frac{\partial \varphi}{\partial t} = D\Delta\varphi$$

where φ is the mud diffusion inside the rubber, D is the diffusion coefficient, and Δ is the Laplacian or Laplace operator.

Fig. 25 displays the simulation of the mud diffusion inside the rubber after a certain time. The red color shows a high percentage of swelling due to diffusion of the mud whereas the blue represents low percentages. In particular, one can understand how different profile and thickness will react to different muds.

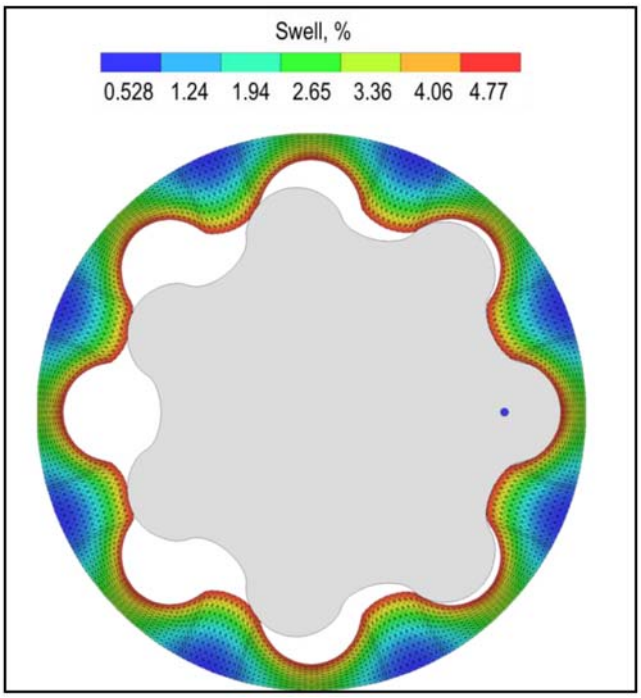

Figure 25—Model showing the mud diffusion inside the rubber after a certain time.

However, the whole process may be much more complicated than shown in Fig. 25 with the chemical reactions and the polymer degradation involved. The polymer chemical degradation, antioxidant leaching, and chain stretching due to the swell usually lead to some degradation of the fatigue properties.

One can see on the graphs of Fig. 26 how much effect the mud can have on the fatigue life of mud motors. The curves are showing a power section fatigue life made of an elastomer fully saturated with a certain water-base mud (WBM) versus the same elastomer non-contaminated by the WBM. The life is expressed in log scale. At high differential pressures, there are several orders of magnitude difference between the two.

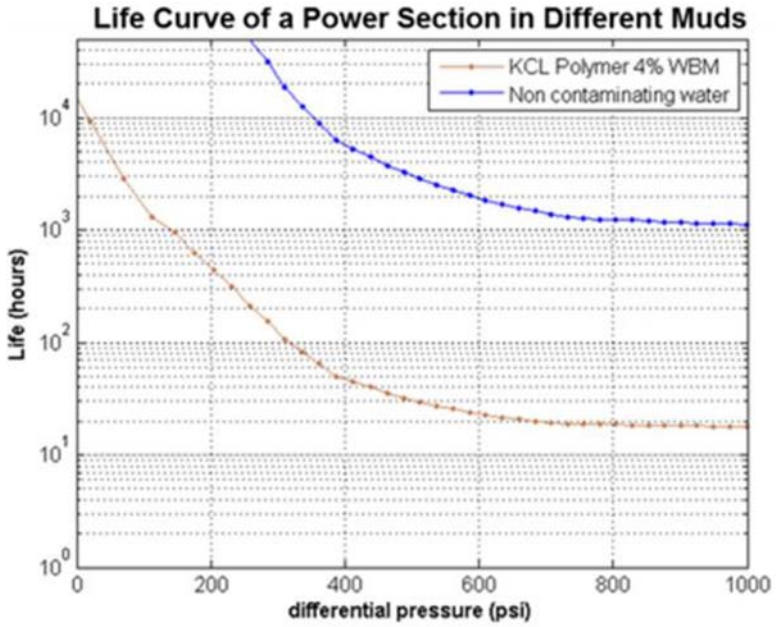

Figure 26—Fatigue life prediction with two different muds.

FSI, 3D Behavior, and Pressure Distribution. It is important to note that the behavior of the power section is 3D. With a simple 2D simulation, one can miss some important behavior of the power section and thus get the wrong answers. Fig. 8c shows the flow path line through the fluid domain enclosed between the stator and the rotor surface. The fluid velocities above the stator surface are shown in Fig. 8d, and pressures are shown in Fig. 8e. One can clearly see in this figure that different sections along the length will have different behavior and the flow through the power section is complex.

To better illustrate this, the rotor and the stator geometry can be revealed unwrapped as a 2D representation according to the angular position and the axial location at the stator surface. Fig. 27 displays the gap between the stator and the rotor surfaces at one of the simulated conditions.

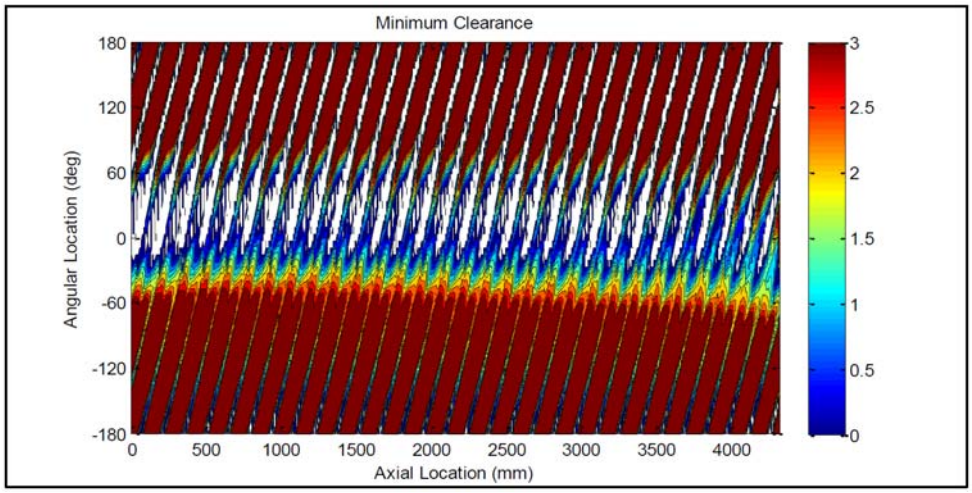

Figure 27—Unwrapped 2D representation of the gap distance between the stator and the rotor seen from the stator.

The zero degree angle (in the Y-axis) is aligned with the main high-pressure horizontal sealing line along the axial direction. For this power section under the simulated conditions, the majority of the cavity boundaries are sealed well with full contact. Gaps exist in the region immediately behind the horizontal

sealing line. As revealed in Fig. 28, the slippage flow that runs through the gap can create higher localized velocities at small gaps. In contrast, the velocities inside the center region of the cavities are relatively low. With the high localized flow velocity, high localized pressure drops can occur.

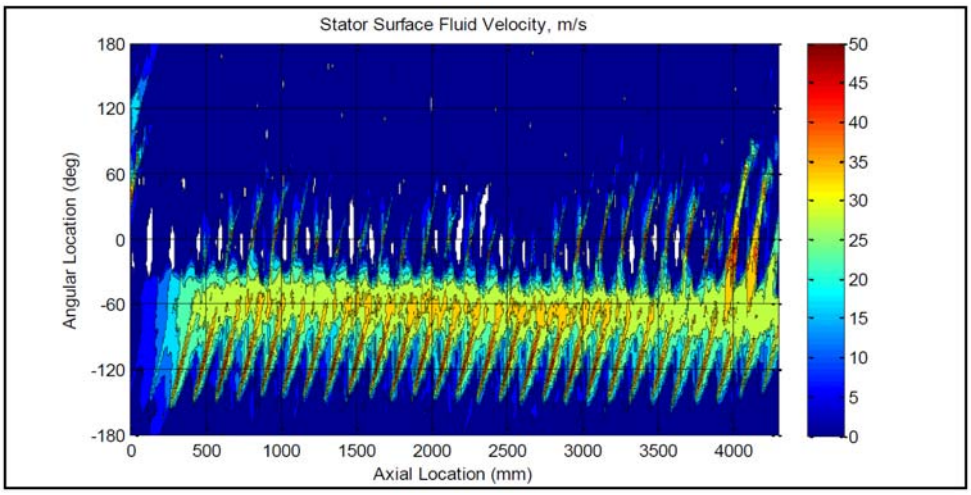

Figure 28—Fluid velocity above the stator surfaces.

It is clear on Fig. 28 that the inlet and the outlet do not exhibit the same features. In particular, the velocities are much higher at the outlet than at the inlet. Consequently, the relative pressure drops will be different between the two. In fact, we found many more features that explain some of the field observations of different performance and reliability measures between the inlet and the outlet.

Fig. 29 displays the static pressure distribution on the stator surface. The pressure inside one cavity is essentially uniform whereas the pressure drops mainly occur at the sealing boundaries where small gaps break the seal. The fluid velocity and pressure distributions on the rotor have very similar trends.

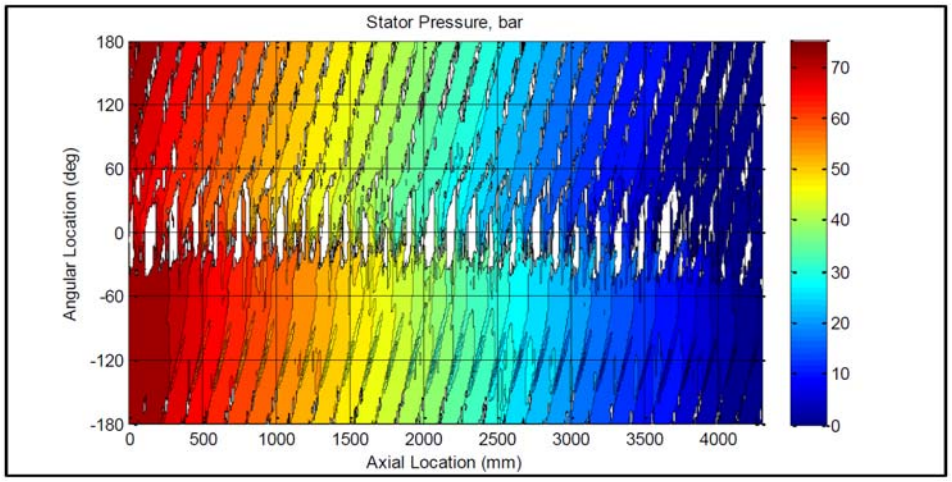

Figure 29—Pressures on the stator surfaces.

The overall FEA, CFD, and FSI scheme has been validated with the IDT presented in section 2.1. In addition, the correlation between the two is very good, as can be seen on the graphs of Fig. 30.

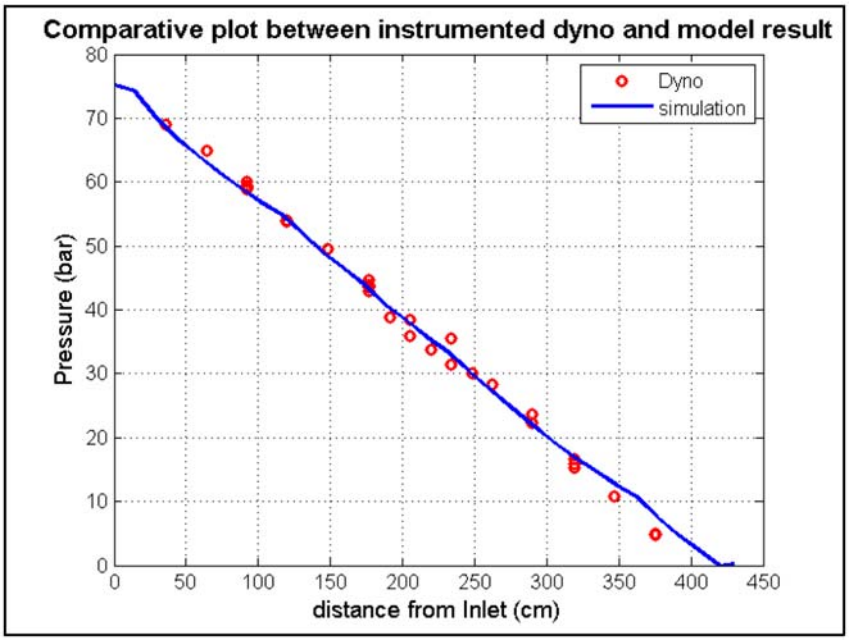

Figure 30—Comparative graph between instrumented dynamometer test and FSI simulation.

The red dots denote the pressure values taken by pressure sensors during the instrumented dynamometer test. Every dot represents a measurement from a pressure sensor. Note that some sensors were located exactly at the same cross section and consequently will have the same distance from the inlet even if they might see different cavities. The blue curve represents the pressure value from the converged solution of the FSI for the same differential pressure. It is important to note that the dynamometer data were shifted to show only the true differential pressure across the motor.

Conclusion

A modeling methodology of downhole mud motor power sections in this study is a combination of analytical and finite element simulations, instrumental testing, and experimental testing. Using this methodology, one can simulate mud motors and predict their power performance, fatigue life, hysteresis heating, and so forth. Many challenges must be overcome to build a proper computational model of power sections involving complex motor kinematics with progressive cavities moving in a spiral motion; unusual contact mechanisms with large nonlinear deformation of elastomer involving hysteresis heating, fluid, and structure interactions; and complicated fluctuating loading conditions downhole. Despite these challenges, the capability of the proposed model has been proven. The methodology compares field, instrumental, and experimental data. An IDT was performed, and elastomer laboratory testing was conducted to provide nonlinear material data. Laser scanning instrumental technology was adopted to obtain the true power section geometry. A combination of analytical, FEA, CFD, and FSI software packages was used to solve the interaction problem between the drilling fluid, the motor structure, and the kinematics.

Using the described modeling methodology, one can simulate mud motors for improving and optimizing power section design, selecting appropriate motors prior to job execution, understanding optimized drilling parameters, performing failure analysis, and rapidly training field personal on motor operations. The capability of this modeling tool in predicting power section performance and fatigue life can be utilized in broad applications from direct field operations, well planning, and motor design to new product/material development. Results of some representative case studies using this powerful tool were discussed.

This methodology applied here for PCPs and PDMs can be used for any other tools made up with elastomers subject to complicated dynamic loadings. Thus, this methodology can be utilized in fields beyond drilling applications or even oilfield applications.

Although we exposed here a comprehensive high-fidelity model for mud motors, some additional work is needed. In particular, we have not discussed here the effect of the mud solid content on the overall reliability of power sections.